

Ordered B-site vacancies in an ABX_3 formate perovskite

Hanna L. B. Boström,^{†,‡} Jonas Bruckmoser,[¶] and Andrew L. Goodwin*,[†]

[†]Department of Chemistry, University of Oxford, Inorganic Chemistry Laboratory, South Parks Road, Oxford OX1 3QR, UK

[‡]Department of Chemistry, Ångström Laboratory, Uppsala University, Box 538, 751 21 Uppsala, Sweden

[¶]Department of Chemistry, Technical University of Munich, Lichtenbergstraße 4, Garching, Germany

Received August 28, 2019; E-mail: andrew.goodwin@chem.ox.ac.uk

Abstract: We report the synthesis and structural characterisation of a series of aliovalently doped metal–formate ABX_3 perovskite frameworks $[C(NH_2)_3]Mn_{1-x}^{2+}(Fe_{2x/3}^{3+}, \square_{x/3})(HCOO)_3$ (\square = B-site vacancy). For sufficiently large x , the vacancies order, lowering the crystal symmetry from orthorhombic $Pnna$ to monoclinic $P2/n$. This system establishes B-site vacancies as a new type of defect in formate perovskites, and one with important chemical, structural, and functional implications. Monte Carlo simulations driven by a nearest-neighbour vacancy repulsion model show checkerboard vacancy order to emerge for $x > 0.6$, in accord with experiment.

Molecular perovskites—coordination polymers with the ABX_3 perovskite stoichiometry and topology—are an important contemporary materials family, as they combine the well-established functionality of the perovskite structure type with the mechanical and compositional flexibility of metal–organic frameworks (MOFs).^{1,2} The organic lead–halide and formate perovskites are probably the best known examples—the former famous for its efficient photovoltaic response, and the latter favoured for its variety of magnetic, dielectric, and ferroelectric behaviour.^{1,3–6}

For conventional inorganic perovskites, the inclusion of vacancies within the ABX_3 structure type has been a crucially important design tool. By way of example, A-site vacancies allow for intercalation chemistry (whether reductive or inert)^{7,8} and negative thermal expansion;^{9,10} vacancies on the X-site can give rise to fast ion conductors,¹¹ and relate the perovskite structure to that of high- T_c superconductors such as $YBa_2Cu_3O_{7-\delta}$.¹² B-site vacancies are much rarer in oxide perovskites, but the discovery of efficient hole transport properties in Cs_2SnI_6 ($\equiv Cs(Sn_{1/2}\square_{1/2})I_3$) has helped refocus attention on this compositional degree of freedom in the halide analogues.¹³ Indeed this family has recently been extended to include the molecular systems A_2PtI_6 (A = organic monocation).¹⁴ The particular motivation for developing B-site vacancy chemistry comes from the prospect for exploiting such vacancies to tune B-site oxidation state, promote low-coordination intercalation, and/or amplify anion–anion interactions.¹⁵

Given the recent discovery that B-site cation substitution is straightforwardly achieved in formate perovskites, we were interested to establish whether this family might support B-site vacancies. An obvious strategy is to employ B^{n+} cations with charges $n > 2$: since the organic A-site cation is nearly always monovalent, charge balance could be achieved by reducing the B-site occupancy to $2/n$. Yet there are relatively few reported examples of formate perovskites containing trivalent B-site cations (and none, of which we are aware, with higher charge states). It is known, for example, that B^{2+} can be substituted for an equimolar mixture of (ordered) B^+/B^{3+} ,^{16–18} but this has the same average charge state and so does

not of course give rise to vacancies. Alternatively, small amounts ($< 15\%$) of Cr^{3+} and other trivalent cations have been included in some dimethylammonium formate perovskites, but in all known cases charge balance is achieved not by incorporating B-site vacancies but by replacement of the A-site cation by neutral formic acid molecules.^{19,20} This resembles the mechanism for charge compensation in oxide perovskites, where aliovalent substitution is usually accompanied by the formation of A-site vacancies. In the formates, higher levels of trivalent substitution $> 15\%$ have so far led to a charge-ordered niccolite structure, rather than A- or B-site deficient perovskites.^{21–25}

It was in this context that we explored aliovalent doping of guanidinium ($C(NH_2)_3^+$) metal–formate perovskites. Guanidinium is noteworthy in the context of hybrid formate perovskites for forming a particularly strong set of six hydrogen bonds with its surrounding formate anions.^{26,27} This contrasts the much weaker cation–framework interactions in dimethylammonium metal formates: the dimethylammonium cation is relatively small and only forms weak hydrogen bonds, resulting in dynamical disorder when encapsulated in either a niccolite or perovskite cage.^{3,27} Guanidinium formates retain orientational order at all accessible temperatures.²⁷ Hence we reasoned that these systems may allow stabilisation of the perovskite topology to larger defect concentrations than is otherwise possible.

We prepared a series of polycrystalline samples of formula $[C(NH_2)_3]Mn_{1-x}^{2+}(Fe_{2x/3}^{3+}, \square_{x/3})(HCOO)_3$ (nominal composition $x_{nom} = 0, 0.05, 0.1, 0.2, \dots, 1.0$) by adapting the method reported in Refs. 26,28. Compositions were determined by atomic absorption spectroscopy (AAS); we found the true values (denoted x) to deviate significantly from the x_{nom} , and so the former is used hereafter. The rapid precipitation methodology we used, together with the absence of any visible colour change, collectively suggest that there was no substantial autoreduction of Fe^{3+} to Fe^{2+} during synthesis.

Using synchrotron powder X-ray diffraction measurements, we explored the phase behaviour of the entire solid solution (see SI for details). We found the endmember $[C(NH_2)_3]Mn(HCOO)_3$ (**1**) to crystallise with orthorhombic $Pnna$ symmetry, as reported in 26. On increasing Fe^{3+} content, this symmetry persists until $x \simeq 0.6$ [Fig. 1(a)]. Beyond this point, the crystal symmetry is lowered from $Pnna$ to the maximal subgroup $P2/n$, as evidenced by the appearance of reflections forbidden in $Pnna$ but allowed in $P2/n$. A non-standard setting of $P2/n$ ($\equiv P2/n11$) is used to allow direct comparison of the unit-cells between the two phases. Group-theoretical analysis gives that the symmetry lowering from $Pnna$ to $P2/n$ must be driven by checkerboard ordering of distinct species at the B-sites. In the case of the Fe-rich endmember $[C(NH_2)_3]Fe_{2/3}(HCOO)_3$ (**2**), for example, this implies that the B-site Fe occupancy alternates between two different values. The relatively narrow peak profiles suggest that whatever drives this symmetry lowering does not lead to any significant strain.

A candidate structural model for **2** could then be derived from

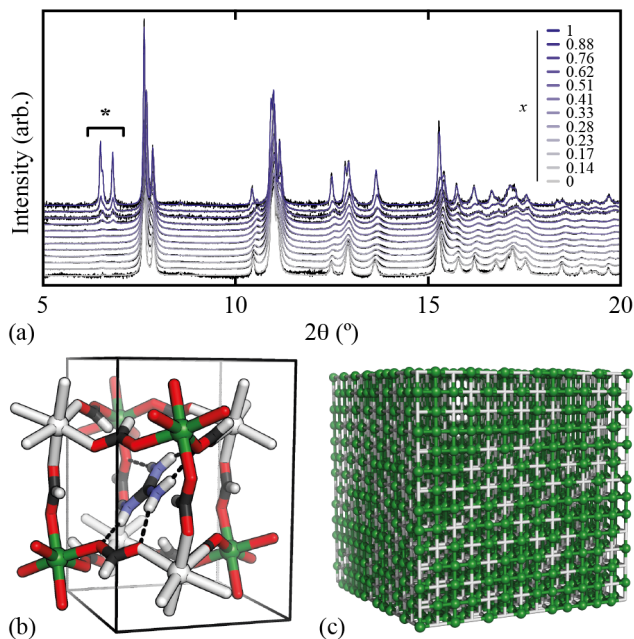


Figure 1. (a) Experimental powder X-ray diffraction patterns (black lines, $\lambda = 0.8248300(1) \text{ \AA}$) and Pawley refinement fits (coloured lines) as a function of composition x in $[\text{C}(\text{NH}_2)_3]\text{Mn}_{1-x}(\text{Fe}_{2x/3}^{3+}, \square_{x/3})(\text{HCOO})_3$. The additional peaks marked by an asterisk are characteristic of symmetry lowering from $Pnna$ to $P2_1/n$, which we find to occur for $x \geq 0.6$. (b) Structural model for **2** discussed in the text. C atoms in black, H in white, N in blue, and O in red. Fully- and partially-occupied Fe sites shown as green and white octahedral nodes, respectively. In the non-standard $P2_1/n11$ setting, the b axis is vertical and the c axis is approximately horizontal. (c) Representative Fe occupancy distribution in **2** as determined by MC simulations: green and white sites indicate Fe centres and vacancies, respectively. Our analysis is not sensitive to the presence or otherwise of formate anions (although from charge balance and hydrogen-bonding perspectives we anticipate few X-site vacancies).

that of **1** (Ref. 26) but with two alternating B-site Fe occupancies of 100% and 33% [Fig. 1(b)]. This model gave an excellent match to our experimental diffraction pattern in Rietveld refinements even without any refinement of the atomic coordinates [see SI]. Alternative models, *e.g.* containing A-site vacancies, do not have the correct crystal symmetry and could not account for our data. Hence our measurements suggest that $[\text{C}(\text{NH}_2)_3]\text{Fe}_{2/3}\square_{1/3}(\text{HCOO})_3$ contains a substantial fraction of B-site vacancies. Indeed the total defect concentration of 33% exceeds that of many other defective metal–organic frameworks and coordination polymers,^{29–32} including even the family of Prussian blue analogues, where as many as one in six B-site cations is missing.^{33–35}

Pawley refinements then allowed us to track structural changes throughout the entire solid solution as Mn^{2+} is replaced by a combination of Fe^{3+} and vacancies [Fig. 1(a)]. The dominant effect is a variation of the normalised cell volume, which first decreases by $\sim 2\%$ within the $Pnna$ phase and subsequently increases for $x \geq 0.6$, just as vacancy order emerges and the crystal symmetry lowers to $P2_1/n$ [Fig. 2]. This deviation from Vegard’s-law behaviour suggests strong effective interactions between the B-site substituents, with anti-clustering of Fe dopants indicated by the volume reduction for maximum mixing ($x \sim 0.5$).³⁶ That both endmembers have very similar molar volumes (231.66(2) and 231.88(3) \AA^3 for $x = 0$ and 1, respectively) means that the effective radius at the vacant B-site is larger than that of Mn^{2+} , since $r(\text{Fe}^{3+}) < r(\text{Mn}^{2+})$. We cannot rule out the possibility that small neutral species, such as H_2O , reside in the vacant B-sites.

Having established the presence of B-site vacancies in

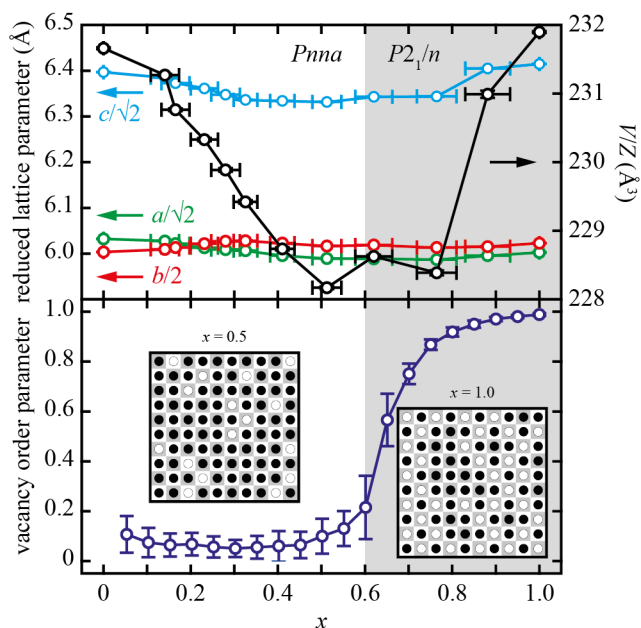


Figure 2. Variation in (top) experimental lattice parameters and reduced cell volume, and (bottom) MC vacancy order parameter with composition x . The transition from disordered $Pnna$ to ordered $P2_1/n$ vacancy arrangements occurs for $x \simeq 0.6$ in both cases. Insets show representative MC simulation sections for $x = 0.5$ and 1.0 ; occupied (vacant) B-sites as black (white) circles, with underlying lattice sites as alternating white and grey tiles. For low x , both types of lattice site contain vacancies; for $x \gtrsim 0.6$ vacancies are distributed on only one sublattice (here, grey).

$[\text{C}(\text{NH}_2)_3]\text{Mn}_{1-x}^{2+}(\text{Fe}_{2x/3}^{3+}, \square_{x/3})(\text{HCOO})_3$, we sought to understand the mechanism of vacancy ordering for $x \geq 0.6$. Since vacancies carry an effective negative charge relative to the average 2+ charge state of the perovskite B-site, we reasoned that short-range vacancy–vacancy repulsions may be the most physical driving force for vacancy order. To test this hypothesis we carried out a series of Monte Carlo (MC) simulations for different B-site vacancy fractions spanning the experimental values of 0–33% ($x = 0$ –1). Our MC configurations represented a $14 \times 14 \times 14$ supercell of the aristotypic perovskite cell. Vacancies of a fixed number were initially distributed randomly throughout these supercells. The configurational energy was determined as a simple sum of the number of nearest-neighbour vacancy–vacancy pairs. We used a combined MC / simulated annealing approach to find a ground state configuration for each vacancy concentration. In seeking to interpret our experiment results in terms of these ground state structures, our assumption is that the actual energy penalty associated with forming vacancy pairs is large with respect to ambient temperature (*i.e.* $\gg 2.5 \text{ kJ mol}^{-1}$). Our simulations show that long-range vacancy order emerges spontaneously for vacancy concentrations $\gtrsim 20\%$ (*i.e.* $x \gtrsim 0.6$). This order splits the B-sites into two symmetry-inequivalent sites, which alternate throughout the lattice and correspond to cation occupancy fractions of 1 and $(1 - 2x/3)$ [Fig. 2]. So this simple model can account for the emergence and nature of vacancy order observed experimentally.

The additional stabilisation mediated by supramolecular hydrogen-bonding interactions likely explains the retention of the perovskite network even in the absence of a large fraction of B-site cations. Taking into account the guanidinium–formate hydrogen bonds, the network structure of **2** is fully connected in three-dimensions, irrespective of the arrangement of Fe atoms on the vacancy-rich B-site [see Fig. 1(c) for a representation of vacancy distributions in **2**]. These results suggest that guanidinium metal–formates should might reasonably be considered

as supramolecular, rather than covalent, frameworks. We note that guanidinium is known for forming a range of supramolecular frameworks, including perovskite-like systems.^{37,38}

The B-site vacancies we identify have several implications for the structural and functional behaviour of the metal–formate perovskites. First, as the metal centres in $[\text{C}(\text{NH}_2)_3]\text{Mn}_{1-x}^{2+}(\text{Fe}_{2x/3}^{3+}\square_{x/3})(\text{HCOO})_3$ are diluted by vacancies, any properties depending on coupling between neighbouring B-site cations are naturally affected. This is relevant to cooperative magnetic and orbital order, for example, both of which are important features of formate perovskite physics.^{28,39–41} Second, the hybrid perovskite family might now be extended to accommodate a larger variety of trivalent cations, which in principle allows for the synthesis of lanthanide-containing analogues and, in turn, new luminescent materials. Third, we expect that B-site vacancies will allow transport phenomena not usually associated with hybrid perovskites. For example, the intercalation of small cations onto the B-site could accompany reduction of Fe^{3+} to Fe^{2+} . Noting the octahedral coordination of Na^+ by formate in $\text{NaMn}(\text{HCOO})_3$,⁴² one might infer the accessibility of mixed-valent Na^+ -intercalated species such as $[\text{C}(\text{NH}_2)_3]\text{Na}_{1/3}\text{Fe}_{2/3}^{2+/3+}(\text{HCOO})_3$. Likewise the proton conductivity behaviour of other formates⁴³ might be enhanced by exploiting cation vacancies. Fourth, we would expect different mechanical and thermal expansion properties in defective and stoichiometric systems.^{44–47} In this context, we note that the network of guanidinium and formate ions in **2** form a herringbone pattern, which is a motif often associated with anomalous elastic phenomena.^{48–50} And, fifth, the symmetry-lowering effect of vacancy order might be exploited to drive hybrid improper ferroelectricity *via* coupling to other distortions, such as orientational order of the A-site cations.^{51,52}

Our results highlight the intriguing chemistry present at the intersection of MOF and perovskite chemistry. Both types of compounds are able to host substantial number of vacancies, yet with different manifestations. Metal–organic frameworks and coordination polymers show a broad variety of defects,^{53–56} but reports of metal vacancies as a result of mixed valence are rare.⁵⁴ The prototypical example of a defective MOF is $\text{UiO}-66$,^{57,58} where the missing-cluster defects aggregate into compositional nanoregions.^{32,59} In oxide perovskites, mixed-valent solid solutions are ubiquitous, yet the charge compensation is more commonly achieved through vacancies on the A-site, rather than the B-site.^{60,61} Here, we have demonstrated how mixed valence in a metal–organic framework with the perovskite architecture results in partially ordered vacancies on the metal B-site. The homogenous vacancy distribution contrasts with the compositional nanoregions of isovalent mixed-metal systems.^{62,63} The high concentration of metal vacancies is facilitated by the guanidinium cation and its strong hydrogen bonding interactions with the anionic formate X-site species. Our results have important implications for the functional response of these materials and suggest that strong hydrogen bonding can play a key role in stabilising a particular structure type.

Acknowledgement We thank Diamond Light Source (I11 Beamline) for the provision of beamtime *via* the Block award grant and C. S. Coates (Oxford) and the I11 beamline staff for the assistance with data collection. ALG gratefully acknowledges financial support from the E.R.C. (Grant 788144).

References

- (1) Li, W.; Wang, Z.; Deschler, F.; Gao, S.; Friend, R. H.; Cheetham, A. K. Chemically diverse and multifunctional hybrid organic-inorganic perovskites. *Nat. Rev. Mater.* **2017**, *2*, 16099.
- (2) Kieslich, G.; Goodwin, A. L. The same and not the same: molecular perovskites and their solid-state analogues. *Mater. Horiz.* **2017**, *4*, 362–366.
- (3) Wang, X.-Y.; Gan, L.; Zhang, S.-W.; Gao, S. Perovskite-like Metal For-

- mates with Weak Ferromagnetism and as Precursors to Amorphous Materials. *Inorg. Chem.* **2004**, *43*, 4615–4625.
- (4) Wang, Z.; Zhang, B.; Otsuka, T.; Inoue, K.; Kobayashi, H.; Kurmoo, M. Anionic NaCl-type frameworks of $[\text{Mn}^{\text{II}}(\text{HCOO})_6]^-$, templated by alkylammonium, exhibit weak ferromagnetism. *Dalton Trans.* **2004**, 2209–2216.
- (5) Jain, P.; Dalal, N. S.; Toby, B. H.; Kroto, H. W.; Cheetham, A. K. Order-Disorder Antiferroelectric Phase Transition in a Hybrid Inorganic–Organic Framework with the Perovskite Architecture. *J. Am. Chem. Soc.* **2008**, *130*, 10450–10451.
- (6) Jain, P.; Ramachandran, V.; Clark, R. J.; Zhou, H. D.; Toby, B. H.; Dalal, N. S.; Kroto, H. W.; Cheetham, A. K. Multiferroic behavior associated with an order–disorder hydrogen bonding transition in metal–organic frameworks (MOFs) with the perovskite ABX_3 architecture. *J. Am. Chem. Soc.* **2009**, *131*, 13625–13627.
- (7) Hägg, G. The Spinel and the Cubic Sodium–Tungsten Bronzes as New Examples of Structures with Vacant Lattice Points. *Nature* **1935**, *135*, 874.
- (8) Hester, B. R.; dos Santos, A. M.; Molaison, J. J.; Hancock, J. C.; Wilkinson, A. P. Synthesis of Defect Perovskites $(\text{He}_{2-x}\square_x)(\text{CaZr})\text{F}_6$ by Inserting Helium into the Negative Thermal Expansion Material CaZrF_6 . *J. Am. Chem. Soc.* **2017**, *139*, 13284–13287.
- (9) Rodriguez, E. E.; Llobet, A.; Proffen, T.; Melot, B. C.; Seshadri, R.; Littlewood, P. B.; Cheetham, A. K. The role of static disorder in negative thermal expansion in ReO_3 . *J. Appl. Phys.* **2009**, *105*, 114901.
- (10) Greve, B. K.; Martin, K. L.; Lee, P. L.; Chupas, P. J.; Chapman, K. W.; Wilkinson, A. P. Pronounced Negative Thermal Expansion from a Simple Structure: Cubic ScF_3 . *J. Am. Chem. Soc.* **2010**, *132*, 15496–15498.
- (11) Norby, T. Fast oxygen ion conductors—from doped to ordered systems. *J. Mater. Chem.* **2001**, *11*, 11–18.
- (12) Jorgensen, J. D.; Veal, B. W.; Paulikas, A. P.; Nowicki, L. J.; Crabtree, G. W.; Claus, H.; Kwok, W. K. Structural properties of oxygen-deficient $\text{YBa}_2\text{Cu}_3\text{O}_{7-\delta}$. *Phys. Rev. B* **1990**, *41*, 1863–1877.
- (13) Lee, B.; Stoumpos, C. C.; Zhou, N.; Hao, F.; Malliakas, C.; Yeh, C.-Y.; Marks, T. J.; Kanatzidis, M. G.; Chang, R. P. H. Air-Stable Molecular Semiconducting Iodosalts for Solar Cell Applications: Cs_2SnI_6 as a Hole Conductor. *J. Am. Chem. Soc.* **2014**, *136*, 15379–15385.
- (14) Evans, H. A.; Fabiani, D. H.; Andrews, J. L.; Koerner, M.; Preefer, M. B.; Wu, G.; Wudl, F.; Cheetham, A. K.; Seshadri, R. Hydrogen Bonding Controls the Structural Evolution in Perovskite-Related Hybrid Platinum (IV) Iodides. *Inorg. Chem.* **2018**, *57*, 10375–10382.
- (15) Evans, H. A.; Andrews, J. L.; Fabiani, D. H.; Preefer, M. B.; Wu, G.; Cheetham, A. K.; Wudl, F.; Seshadri, R. The capricious nature of iodine catenation in I_2 excess, perovskite-derived hybrid Pt(IV) compounds. *Chem. Commun.* **2019**, 55, 588–591.
- (16) Plutecka, A.; Rychlewska, U. A three-dimensional Al(III)/Na(I) metal-organic framework resulting from dimethylformamide hydrolysis. *Acta Crystallogr., Sect. C: Cryst. Struct. Commun.* **2009**, *65*, m77.
- (17) Yu, Y.; Shang, R.; Chen, S.; Wang, B.-W.; Wang, Z.-M.; Gao, S. A Series of Bimetallic Ammonium AlNa Formates. *Chem. Eur. J.* **2017**, *23*, 9857–9871.
- (18) Ptak, M.; Gągor, A.; Sieradzki, A.; Bondzior, B.; Dereń, P.; Ciupa, A.; Trzebiatowska, M.; Mączka, M. Effect of K^+ cations on phase transitions, structural, dielectric and luminescent properties of $[\text{cat}][\text{K}_{0.5}\text{Cr}_{0.5}(\text{HCOO})_3]$, where cat is protonated dimethylamine or ethylamine. *Phys. Chem. Chem. Phys.* **2017**, *19*, 12156–12166.
- (19) Mączka, M.; Gągor, A.; Hermanowicz, K.; Sieradzki, A.; Macalik, L.; Pikul, A. Structural, magnetic and phonon properties of Cr(III)-doped perovskite metal formate framework $[(\text{CH}_3)_2\text{NH}_2][\text{Mn}(\text{HCOO})_3]$. *J. Solid State Chem.* **2016**, *237*, 150–158.
- (20) Mączka, M.; Sieradzki, A.; Bondzior, B.; Dereń, P.; Hanuza, J.; Hermanowicz, K. Effect of aliovalent doping on the properties of perovskite-like multiferroic formates. *J. Mater. Chem. C* **2015**, *3*, 9337–9345.
- (21) Mączka, M.; Pietraszko, A.; Pikul, A.; Hermanowicz, K. Luminescence, magnetic and vibrational properties of novel heterometallic niccolites $[(\text{CH}_3)_2\text{NH}_2][\text{Cr}^{\text{III}}\text{M}^{\text{II}}(\text{HCOO})_6]$ ($\text{M}^{\text{II}} = \text{Zn}, \text{Ni}, \text{Cu}$) and $[(\text{CH}_3)_2\text{NH}_2][\text{Al}^{\text{III}}\text{Zn}^{\text{II}}(\text{HCOO})_6] \cdot \text{Cr}^{3+}$. *J. Solid State Chem.* **2016**, *233*, 455–462.
- (22) Hagen, K. S.; Naik, S. G.; Hanh Huynh, B.; Masello, A.; Christou, G. Intensely colored mixed-valence iron(II) iron(III) formate analogue of Prussian Blue exhibits Neel N-type ferrimagnetism. *J. Am. Chem. Soc.* **2009**, *131*, 7516–7517.
- (23) Zhao, J.-P.; Hu, B.-W.; Lloret, F.; Tao, J.; Yang, Q.; Zhang, X.-F.; Bu, X.-H. Magnetic Behavior Control in Niccolite Structural Metal Formate Frameworks $[\text{NH}_2(\text{CH}_3)_2][\text{Fe}^{\text{III}}\text{M}^{\text{II}}(\text{HCOO})_6]$ ($\text{M} = \text{Fe}, \text{Mn}, \text{and Co}$) by Varying the Divalent Metal Ions. *Inorg. Chem.* **2010**, *49*, 10390–10399.
- (24) Mączka, M.; Kucharska, E.; Gągor, A.; Pikul, A.; Hanuza, J. Synthesis, magnetic and vibrational properties of two novel mixed-valence iron(II)-iron(III) formate frameworks. *J. Solid State Chem.* **2018**, *258*, 163–169.
- (25) Sieradzki, A.; Pawlus, S.; Tripathy, S. N.; Gągor, A.; Ciupa, A.; Mączka, M.; Paluch, M. Dielectric relaxation behavior in antiferroelectric metal organic framework $[(\text{CH}_3)_2\text{NH}_2][\text{Fe}^{\text{III}}\text{Fe}^{\text{II}}(\text{HCOO})_6]$ single crystals. *Phys. Chem. Chem. Phys.* **2016**, *18*, 8462–8467.
- (26) Hu, K.-L.; Kurmoo, M.; Wang, Z.; Gao, S. Metal–Organic Perovskites: Synthesis, Structures, and Magnetic Properties of $[\text{C}(\text{NH}_2)_3][\text{M}^{\text{II}}(\text{HCOO})_3]$ ($\text{M} = \text{Mn}, \text{Fe}, \text{Co}, \text{Ni}, \text{Cu}, \text{and Zn}$; $\text{C}(\text{NH}_2)_3 = \text{Guanidinium}$). *Chem. Eur. J.* **2009**, *15*, 12050–12064.
- (27) Svane, K. L.; Forse, A. C.; Grey, C. P.; Kieslich, G.; Cheetham, A. K.; Walsh, A.; Butler, K. T. How Strong is the Hydrogen Bond in Hybrid Perovskites? *J. Phys. Chem. Lett.* **2017**, *8*, 6154–6159.
- (28) Evans, N. L.; Thygesen, P. M. M.; Boström, H. L. B.; Reynolds, E. M.; Collings, I. E.; Phillips, A. E.; Goodwin, A. L. Control of Multipolar and

- Orbital Order in Perovskite-like $[\text{C}(\text{NH}_2)_3]\text{Cu}_x\text{Cd}_{1-x}(\text{HCOO})_3$ Metal–Organic Frameworks. *J. Am. Chem. Soc.* **2016**, *138*, 9393–9396.
- (29) Tu, B.; Pang, Q.; Wu, D.; Song, Y.; Weng, L.; Li, Q. Ordered vacancies and their chemistry in metal–organic frameworks. *J. Am. Chem. Soc.* **2014**, *136*, 14465–14471.
 - (30) Shen, L.; Yang, S.-W.; Xiang, S.; Liu, T.; Zhao, B.; Ng, M.-F.; Göetlicher, J.; Yi, J.; Li, S.; Wang, L.; Ding, J.; Chen, B.; Wei, S.-H.; Feng, Y. P. Origin of long-range ferromagnetic ordering in metal–organic frameworks with antiferromagnetic dimeric-Cu(II) building units. *J. Am. Chem. Soc.* **2012**, *134*, 17286–17290.
 - (31) Barin, G.; Krungleviciute, V.; Gutov, O.; Hupp, J. T.; Yildirim, T.; Farha, O. K. Defect creation by linker fragmentation in metal–organic frameworks and its effects on gas uptake properties. *Inorg. Chem.* **2014**, *53*, 6914–6919.
 - (32) Cliffe, M. J.; Wan, W.; Zou, X.; Chater, P. A.; Kleppe, A. K.; Tucker, M. G.; Wilhelm, H.; Funnell, N. P.; Coudert, F.-X.; Goodwin, A. L. Correlated defect nanoregions in a metal–organic framework. *Nat. Commun.* **2014**, *5*, 4176.
 - (33) Buser, H. J.; Schwarzenbach, D.; Petter, W.; Ludi, A. The Crystal Structure of Prussian Blue: $\text{Fe}_4[\text{Fe}(\text{CN})_6]_3 \cdot x\text{H}_2\text{O}$. *Inorg. Chem.* **1977**, *16*, 2704–2710.
 - (34) Yamada, S.; Kuwabara, K.; Koumoto, K. Characterization of Prussian Blue analogue: Nanocrystalline nickel–iron cyanide. *Mater. Sci. Eng.* **1997**, *B49*, 89–94.
 - (35) Wardecki, D.; Ojwang, D. O.; Grins, J.; Svensson, G. Neutron Diffraction and EXAFS Studies of $\text{K}_{2x/3}\text{Cu}[\text{Fe}(\text{CN})_6]_{2/3} \cdot n\text{H}_2\text{O}$. *Cryst. Growth Des.* **2017**, *17*, 1285–1292.
 - (36) Castellanos, M.; West, A. R. Deviations from Vegard’s Law in Oxide Solid Solutions. *J. Chem. Soc., Faraday Trans. 1* **1980**, *76*, 2159–2169.
 - (37) White, N. G. Recent advances in self-assembled amidinium and guanidinium frameworks. *Dalton Trans.* **2019**, *48*, 7062–7068.
 - (38) Black, C.; Lightfoot, P. Crystal structure of guanidinium hexafluoridovanadate(III), $(\text{CN}_3\text{H}_6)_3[\text{VF}_6]$: an unusual hybrid compound related to perovskite. *Acta Crystallogr., Sect. C: Struct. Chem.* **2017**, *73*, 244–246.
 - (39) Pato-Doldán, B.; Gómez-Aguirre, L. C.; Bermúdez-García, J. M.; Sánchez-Andújar, M.; Fondado, A.; Mira, J.; Castro-García, S.; Señaris-Rodríguez, M. A. Coexistence of magnetic and electrical order in the new perovskite-like $(\text{C}_3\text{N}_2\text{H}_5)\text{Mn}(\text{HCOO})_3$ formate. *RSC Adv.* **2013**, *3*, 22404–22411.
 - (40) Gómez-Aguirre, L. C.; Pato-Doldán, B.; Mira, J.; Castro-García, S.; Señaris-Rodríguez, M. A.; Sánchez-Andújar, M.; Singleton, J.; Zapf, V. S. Magnetic Ordering-Induced Multiferroic Behavior in $[\text{CH}_3\text{NH}_3][\text{Co}(\text{HCOO})_3]$ Metal–Organic Framework. *J. Am. Chem. Soc.* **2016**, *138*, 1122–1125.
 - (41) Stroppa, A.; Jain, P.; Barone, P.; Marsman, M.; Perez-Mato, J. M.; Cheetham, A. K.; Kroto, H. W.; Picozzi, S. Electric control of magnetization and interplay between orbital ordering and ferroelectricity in a multiferroic metal–organic framework. *Angew. Chem. Int. Ed.* **2011**, *50*, 5847–5850.
 - (42) Paredes-García, V.; Rojas, I.; Madrid, R.; Vega, A.; Navarro-Moratalla, E.; Cañón-Mancisidor, W.; Spodine, E.; Venegas-Yazigi, D. Structural and magnetic characterization of the tridimensional network $[\text{Fe}(\text{HCO}_2)_3]_n \cdot n\text{HCO}_2\text{H}$. *New J. Chem.* **2013**, *37*, 2120–2127.
 - (43) Sieradzki, A.; Pawlus, S.; Tripathy, S. N.; Gagor, A.; Ptak, M.; Paluch, M.; Mączka, M. Dielectric relaxation and anhydrous proton conduction in $[\text{C}_2\text{H}_5\text{NH}_3][\text{Na}_{0.5}\text{Fe}_{0.5}(\text{HCOO})_3]$ metal–organic frameworks. *Dalton Trans.* **2017**, *46*, 3681–3687.
 - (44) Cliffe, M. J.; Hill, J. A.; Murray, C. A.; Coudert, F.-X.; Goodwin, A. L. Defect-dependent colossal negative thermal expansion in $\text{UiO}-66(\text{Hf})$ metal–organic framework. *Phys. Chem. Chem. Phys.* **2015**, *17*, 11586–11592.
 - (45) Zheng, B.; Fu, F.; Wang, L. L.; Wang, J.; Du, L.; Du, H. Effect of Defects on the Mechanical Deformation Mechanisms of Metal–Organic Framework-5: A Molecular Dynamics Investigation. *J. Phys. Chem. C* **2018**, *122*, 4300–4306.
 - (46) Thornton, A. W.; Babarao, R.; Jain, A.; Trouselet, F.; Coudert, F.-X. Defects in metal–organic frameworks: A compromise between adsorption and stability? *Dalton Trans.* **2016**, *45*, 4352–4359.
 - (47) Dissegna, S.; Vervoorts, P.; Hobday, C. L.; Düren, T.; Daisenberger, D.; Smith, A. J.; Fischer, R. A.; Kieslich, G. Tuning the Mechanical Response of Metal–Organic Frameworks by Defect Engineering. *J. Am. Chem. Soc.* **2018**, *140*, 11581–11584.
 - (48) Cairns, A. B.; Goodwin, A. L. Negative linear compressibility. *Phys. Chem. Chem. Phys.* **2015**, *17*, 20449–20465.
 - (49) Prawer, S.; Smith, T. F.; Finlayson, T. R. The Room-Temperature Elastic Behavior of CsH_2PO_4 . *Aust. J. Phys.* **1985**, *38*, 63–83.
 - (50) Shepherd, H. J.; Palamarcu, T.; Rosa, P.; Guionneau, P.; Molnár, G.; Létard, J.-F.; Bousseksou, A. Antagonism between extreme negative linear compression and spin crossover in $[\text{Fe}(\text{dpp})_2(\text{NCS})_2] \cdot \text{py}$. *Angew. Chem.* **2012**, *51*, 3910–3914.
 - (51) Benedek, N. A.; Fennie, C. J. Hybrid improper ferroelectricity: A mechanism for controllable polarization–magnetization coupling. *Phys. Rev. Lett.* **2011**, *106*, 107204.
 - (52) Boström, H. L. B.; Senn, M. S.; Goodwin, A. L. Recipes for improper ferroelectricity in molecular perovskites. *Nat. Commun.* **2018**, *9*, 2380.
 - (53) Sholl, D. S.; Lively, R. P. Defects in Metal–Organic Frameworks: Challenge or Opportunity? *J. Phys. Chem. C* **2015**, *6*, 3437–3444.
 - (54) Cheetham, A. K.; Bennett, T. D.; Coudert, F.-X.; Goodwin, A. L. Defects and disorder in metal organic frameworks. *Dalton Trans.* **2016**, *45*, 4113–4126.
 - (55) Bennett, T. D.; Cheetham, A. K.; Fuchs, A. H.; Coudert, F.-X. Interplay between defects, disorder and flexibility in metal–organic frameworks. *Nat. Chem.* **2017**, *9*, 11–16.
 - (56) Dissegna, S.; Epp, K.; Heinz, W. R.; Kieslich, G.; Fischer, R. A. Defective Metal–Organic Frameworks. *Adv. Mater.* **2018**, 1704501.
 - (57) Cavka, J. H.; Jakobsen, S.; Olsbye, U.; Guilloi, N.; Lamberti, C.; Bordiga, S.; Lillerud, K. P. A New Zirconium Inorganic Building Brick Forming Metal Organic Frameworks with Exceptional Stability. *J. Am. Chem. Soc.* **2008**, *130*, 13850–13851.
 - (58) Wu, H.; Chua, Y. S.; Krungleviciute, V.; Tyagi, M.; Chen, P.; Yildirim, T.; Zhou, W. Unusual and highly tunable missing-linker defects in zirconium metal–organic framework UiO-66 and their important effects on gas adsorption. *J. Am. Chem. Soc.* **2013**, *135*, 10525–10532.
 - (59) Liu, L.; Chen, Z.; Wang, J.; Zhang, D.; Zhu, Y.; Ling, S.; Huang, K. W.; Belmabkhout, Y.; Adil, K.; Zhang, Y.; Slater, B.; Eddaoudi, M.; Han, Y. Imaging defects and their evolution in a metal–organic framework at sub-unit-cell resolution. *Nature Chem.* **2019**, *11*, 622–628.
 - (60) Yoshioka, H. Structure and electrical properties of A-site-deficient perovskite compounds in the $\text{La}_{2/3}\text{TiO}_3$ – $\text{La}_{1/3}\text{NbO}_3$ system. *J. Am. Ceram. Soc.* **2002**, *85*, 1339–1341.
 - (61) Stramare, S.; Thangadurai, V.; Weppner, W. Lithium Lanthanum Titanates: A Review. *Chem. Mater.* **2003**, *15*, 3974–3990.
 - (62) Donlan, E. A.; Boström, H. L. B.; Geddes, H. S.; Reynolds, E. M.; Goodwin, A. L. Compositional Nanodomain Formation in Hybrid Formate Perovskites. *Chem. Commun.* **2017**, *53*, 11233–11236.
 - (63) Šimėnas, M.; Ciupa, A.; Usevičius, G.; Aidas, K.; Klose, D.; Jeschke, G.; Mączka, M.; Völkel, G.; Pöppel, A.; Banys, J. Electron paramagnetic resonance of copper doped $[(\text{CH}_3)_2\text{NH}_2][\text{Zn}(\text{HCOO})_3]$ hybrid perovskite framework. *Phys. Chem. Chem. Phys.* **2018**, *20*, 12097–12105.